

Prediction of CO₂ reduction reaction intermediates and products on transition metal-doped γ -GeSe monolayers: A combined DFT and machine learning approach

Xuxin Kang,^a Wenjing Zhou,^a Ziyuan Li,^a Zhaoqin Chu,^b Hanqin Yin,^c Shan Gao,^a Aijun Du,^{c,*}
Xiangmei Duan^{a,*}

^a School of Physical Science and Technology, Ningbo University, Ningbo, 315211, China.

^b Zhejiang Key Laboratory of Data-Driven High-Safety Energy Materials and Applications, Advanced Interdisciplinary Sciences Research (AiR) Center, Ningbo Institute of Materials Technology and Engineering, Chinese Academy of Sciences, Ningbo 315201, China.

^c School of Chemistry and Physics and Centre for Materials Science, Queensland University of Technology, Gardens Point Campus, Brisbane, QLD 4001, Australia

Email: aijun.du@qut.edu.au, duanxiangmei@nbu.edu.cn Tel: 13429322782

Abstract

The electrocatalytic CO₂ reduction reaction (CO₂RR) is a complex multi-proton-electron transfer process that generates a vast network of reaction intermediates. Accurate prediction of free energy changes (ΔG) of these intermediates and products is essential for evaluating catalytic performance. We combined density functional theory (DFT) and machine learning (ML) to screen 25 single-atom catalysts (SACs) on defective γ -GeSe monolayers for CO₂ reduction to methanol, methane, and formic acid. Among nine ML models evaluated with 14 intrinsic and DFT-based features, the XGBoost performed best ($R^2 = 0.92$ and MAE = 0.24 eV), aligning closely with DFT calculations and identifying Ni, Ru, and Rh@GeSe as prospective catalysts. Feature importance analysis in free energy and product predictions highlighted the significance of CO₂ activation with $\angle O-C-O$ and IP^{C-O1} as the key attributes. Furthermore, by incorporating non-DFT-based features, rapid predictions became possible, and the XGBoost model retained its predictive performance with $R^2 = 0.89$ and MAE = 0.29 eV. This accuracy was further validated using Ir@GeSe. Our work highlights effective SACs for CO₂RR, and provides valuable insights for efficient catalyst design.

1. Introduction

The rapid depletion of fossil fuels has driven an unprecedented surge in greenhouse gas emissions, exacerbating concerns regarding sea-levels rising and global warming. Elevated CO₂ levels, the primary contributor to the greenhouse effect, pose a grave threat to human and ecological health. To address this, sustainable strategies for CO₂ capture and conversion are urgently needed.¹⁻⁶ Electrochemical CO₂ reduction reaction (CO₂RR) to valuable chemicals and fuels stands out as a green and promising approach.⁷⁻⁹ However, CO₂RR involves a complex multi-proton-electron transfer (MPET) process, yielding many different products such as CO, formic acid (HCOOH), methanol (CH₃OH), and methane (CH₄). Despite advances in diverse materials, challenges in catalytic selectivity and activity persists due to the intricate reaction pathways and the high stability of CO₂ molecule requiring significant activation energy. Additionally, competitive hydrogen evolution reactions (HER) can dominate, and thus impede the CO₂RR at higher voltages. Therefore, the development of environmentally friendly catalysts with enhanced efficiency for CO₂RR is a critical research priority.¹⁰⁻¹⁵

Since their inception in 1978, metal-support interactions (MSIs) have garnered considerable attention for modulating the electronic and catalytic properties of catalysts.¹⁶ Recently, MSIs have obtained renewed interest in single atom catalysts (SACs), where isolated metal atoms are stabilized on pristine or defective substrates.¹⁷⁻²¹ The strength of MSIs, influenced by the substrate's charge transfer and coordination environment, alters the electronic states of transition metal (TM) atoms, significantly affecting catalytic performance. For instance, Xun et al. reported a limiting potential (U_L) of -1.24 V for CO₂ reduction to CH₄ on a Ni supported MoSi₂N₄ monolayer,²² while Kou et al. achieved lower potentials of -0.36 V and -0.43 V for Ni and Rh supported In₂Se₃ monolayers.²³ Lei et al. demonstrated exceptional HCOOH selectivity with a U_L of -0.31 V for a single Ni atom anchored on defective phosphorene monolayer, compared to a higher U_L of -0.98 V for producing CH₄,²⁴ and the Pan group reported U_L values of -0.29 V, -0.75 V, and -0.74 V for producing HCOOH, CH₄, and CH₃OH on Ni, Ru, and Rh anchored Ti₂CO₂.²⁵ These findings underscore the importance of substrate selection in the design of SACs. However, the limited understanding of the CO₂RR mechanism and factors governing catalytic activity complicates the development of efficient catalysts. Identifying accessible descriptors to accurately predict the free energy changes of intermediates and products is essential for high-throughput screening of catalysts with improved catalytic activity and selectivity.

To date, research on group IV-VI compounds has primarily focused on the α -phase, akin to black phosphorus, known for its strong in-plane ferroelectric polarization. However, Zou et al.

theoretically predicted a novel γ -phase structure with a four-atomic-layer thickness and unique band dispersion,²⁶ later synthesized by Kim et al as a 2D γ -phase GeSe monolayer via chemical vapor deposition.²⁷ Unlike the conventional α - and β -phases, γ -GeSe exhibits a narrower bandgap and exceptional electronic conductivity, rivaling even most semi-metallic layered materials and surpassing graphite.²⁷ Subsequent studies have explored its electrical, optical, thermal, and thermoelectric properties in pristine, strained, and defective γ -GeSe monolayers.²⁸⁻³² Cai et al. further proposed the γ -GeSe monolayer as a high-capacity anode for lithium-ion batteries due to its low diffusion barrier and excellent conductivity.³³ Inspired by these properties, we hypothesize that the defective γ -GeSe monolayer is a promising substrate for supporting SACs towards efficient CO₂RR.

In this work, we systematically evaluated 25 TMs from the 3d, 4d, and 5d series anchored on defective γ -GeSe monolayers (denoted as TM@GeSe) for CO₂ reduction to C1 products, using DFT and ML models. Through rigorous evaluation of their stability, CO₂ activation, selectivity, and activity, Ni, Ru, and Rh@GeSe emerged as top candidate catalysts for CO₂RR. We trained ML models using two schemes: one with 14 features, including intrinsic and DFT-based (IF+DFT), the other with only 11 intrinsic features (IF), testing nine algorithms on 196 free energy values, and found XGBoost model exhibited exceptional predictive performance for both schemes. Additionally, we defined the producing probability (P) and employed the XGBoost model to predict products. Our work offers a robust framework in catalyst design through rapid, and accurate predictions.

2. Calculation methods

The spin-polarized DFT calculations were performed using the Vienna *Ab initio* Simulation Package (VASP) with the projector-augmented wave (PAW) method.³⁴⁻³⁵ The Perdew-Burke-Ernzerhof (PBE) exchange-correlation functional within the generalized gradient approximation (GGA) was employed.³⁶ A cutoff energy of 520 eV was applied, and the convergence criteria were set as 10^{-5} eV for energy and 0.01 eV/Å for force. The first Brillouin zone was sampled using a $3\times 3\times 1$ Monkhorst–pack k -point grid for structure relaxation and a $6\times 6\times 1$ grid for density of states calculation. To avoid periodic interaction effects, a vacuum space of approximately 15 Å along the z -direction was incorporated. The van der Waals D3 (DFT+D3) correction was applied for accurate modeling of small molecule adsorption.³⁷ Charge density difference and Bader charge analysis were implemented to illustrate the charge transfer. The strength of the chemical bond between CO₂ and TMs was evaluated using the projected crystal orbital Hamilton population (pCOHP) obtained by the LOBSTER code.³⁸ To evaluate the diffusion ease of TMs between vacancies, the diffusion

barriers of TMs were determined based on the climbing image-nudged elastic band (CI-NEB) method.³⁹ Phonon spectrum of γ -GeSe monolayer was calculated using the PHONOPY program with a $4 \times 4 \times 1$ supercell. *Ab initio* molecular dynamics simulations (AIMD) were conducted at 500 K with a total time step of 10 ps to assess the thermodynamic stability of SACs.

The ΔG of every fundamental step of CO₂RR was obtained based on the computational hydrogen electrode (CHE) model proposed by Nørskov et al.⁴⁰ Detailed calculation process can be found in the Supporting Information. The implicit solvation models in VASPsol were constructed to examine the effect of solvation on catalytic activity, employing a dielectric constant of 80 for water.⁴¹

All ML algorithms, including Artificial neural networks (ANNs),⁴² Gradient boosting regression (GBR),⁴³ Extreme gradient boosting regression (XGBoost),⁴⁴ Least absolute shrinkage and selection operator (LASSO),⁴⁵ Support vector regression (SVR),⁴⁶ Decision-trees (DT),⁴⁷ Extra-trees (ET),⁴⁸ K-nearest neighbor (KNN),⁴⁹ Random forest regression (RFR),⁵⁰ were executed using the open-source Scikit-learn library within a Python3 environment.⁵¹ The datasets, collected through DFT calculations, were randomly split into training and test sets with a ratio of 80:20. To assess the performance of these models, we selected three key metrics: coefficient of determination values (R^2), mean absolute error (MAE), and root-mean-square error (RMSE), as outlined in the following equation:

$$R^2 = 1 - \frac{\sum_{i=1}^n (\hat{y}_i - y_i)^2}{\sum_{i=1}^n (\bar{y}_i - y_i)^2} \quad (1)$$

$$\text{MAE} = \frac{1}{n} \sum_{i=1}^n |y_i - \hat{y}_i| \quad (2)$$

$$\text{RMSE} = \sqrt{\frac{1}{n} \sum_{i=1}^n |y_i - \hat{y}_i|^2} \quad (3)$$

where \hat{y}_i represents the i -th calculated value by DFT, y_i means the i -th predicted value by ML model, and \bar{y}_i denotes the average value of DFT calculation results.

3. Results and Discussion

We selected the 2D γ -phase GeSe monolayer as a potential substrate for SACs on three compelling factors: Firstly, the γ -phase is the ground state, exhibiting a total energy lower by 0.31 eV and 0.51 eV compared to the α - and β -phases, respectively, aligning with previous reports.²⁶ Secondly, the remarkable electronic conductivity has been experimentally demonstrated in synthesized γ -phase GeSe monolayers,²⁷ which is confirmed in the calculated energy band diagram in Figure S1(a). Thirdly, its exceptional dynamical stability is evidenced by the absence of imaginary frequencies in the phonon spectrum, as depicted in Figure S1(b).

As illustrated in Figure S2(a), the optimized γ -GeSe monolayer features a distinctive sandwich structure composed of two interconnected single-layer honeycomb lattices. The calculated lattice constants are $a = b = 3.79 \text{ \AA}$, with a thickness of 4.69 \AA , and the bond lengths of Ge–Se and Ge–Ge are 2.58 \AA and 2.95 \AA , respectively, which are consistent with previous studies.^{30, 32}

For efficient CO_2 reduction, effective capture and activation of CO_2 molecules on the catalyst surface are crucial. However, as depicted in Figure S3, when the CO_2 molecule is adsorbed on either Se or Ge atoms, it retains its linear structure, suggesting that the pristine 2D γ -GeSe monolayer may not be an effective catalyst for CO_2RR .

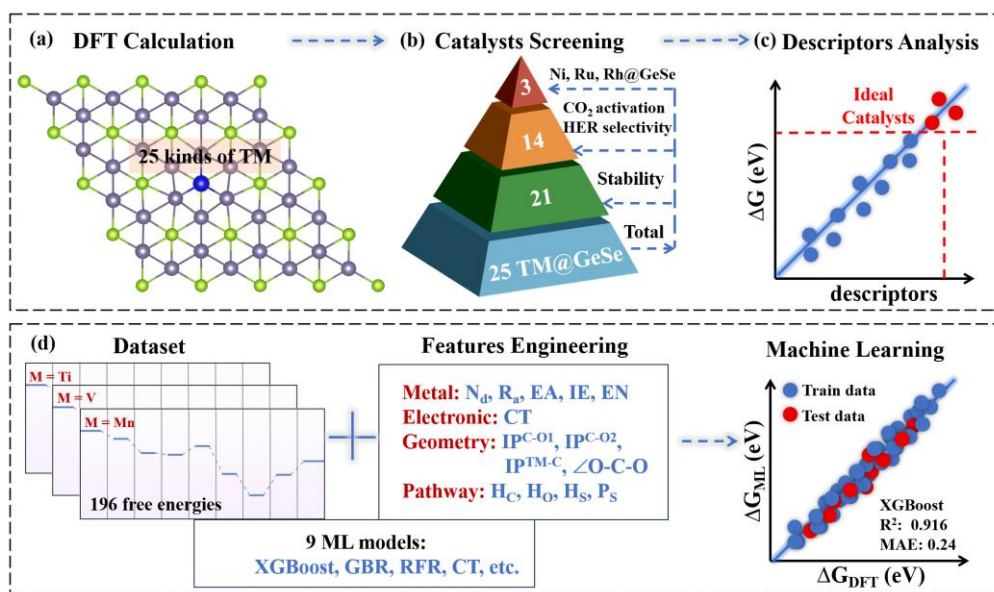


Figure 1. The flowchart used in the work. (a) The construction of 25 different single-atom catalysts. (b) Screening process of promising catalysts. (c) Analysis of key descriptors affecting ΔG values of intermediates. (d) Flow of the machine learning approach.

3.1 Structure and Stability of SACs

We consider anchoring TMs into a single Se vacancy (V_{Se}) on the $4 \times 4 \times 1$ GeSe monolayer (Figure 1a), where TMs supply additional electrons to break the strong sp hybridization. The formation energy (E_f) of V_{Se} was calculated to be 1.3 eV , comparable to those of $V_{\text{S}}\text{-MoS}_2$, $V_{\text{Se}}\text{-MoSe}_2$, and $V_{\text{Se}}\text{-InSe}$,⁵²⁻⁵⁴ and significantly lower than that of V_{C} in graphene and BC_3 .⁵⁵⁻⁵⁶ This suggests the feasibility of V_{Se} formation.

A total of 25 SACs were constructed, and their stability, activity, and selectivity were rigorously evaluated, leading to the identification of the most promising candidates (Figure 1b). The interactions between TMs and substrate were evaluated by calculating the binding energy (E_b). As shown in Table S1, all SACs exhibited considerably negative E_b compared to previously proposed SACs,⁵⁷⁻⁵⁸ indicating a high thermodynamic stability of TM@GeSe . To further assess the tendency of metal atoms to aggregate into clusters, the ratio between E_b and cohesive energy (E_c) was

calculated. The relatively high E_b/E_c values, ranging from 0.6 to 1.19, indicated that TMs preferred to remain isolated on the substrate.^{56, 59}

To substantiate the practical feasibility of TM@GeSe, Ni, Ru, and Rh@GeSe (Figure S4) were exemplified, and the diffusion barriers of TMs across adjacent vacancies were computed. The corresponding diffusion barriers were as high as 2.01 eV, 1.80 eV, and 4.20 eV, respectively, indicating effective inhibition of TM aggregation.²³ As displayed in Figure S5, the energy and temperature simulated by AIMD at 500 K oscillated only slightly around the equilibrium positions, and the structures did not manifest significant deformation or fracture after running 10 ps, revealing high thermodynamic stability and the potential for experimental synthesis of TM@GeSe.^{20, 23, 60} Furthermore, the electrochemical stability was evaluated by computing the dissolution potential (U_{diss}), where positive values indicate that the metal atoms will not detach from the substrate and dissolve into the electrolyte under acidic conditions.⁶¹⁻⁶² As evident from Table S1, most SACs exhibited superior electrochemical stability, except for Sc, Y, Zr, and Hf@GeSe, which were not further elaborated upon.

3.2 Adsorption and Activation of CO₂ Molecules

The CO₂ molecules can bind to TMs in different adsorption modes, including physisorption, end-on, side-on1, and side-on2, as displayed in Figure 2(a). The optimized structure and parameters of CO₂ adsorption, such as TM–C and TM–O1 bond lengths, C–O1 and C–O2 bond lengths, and $\angle\text{O–C–O}$ bond angles, are summarized in Table S2 and Figure S6.

Weak physisorption can occur on Pt and Au, evidenced by the large distance (more than 3 Å) between the TMs and CO₂ molecules. The C–O bond lengths and $\angle\text{O–C–O}$ bond angles are close to 1.17 Å and 180° of free CO₂ gas molecules, respectively. As depicted in Figure 2(b), electron transfer between Pt@GeSe and CO₂ is negligible.

CO₂ can also form weak adsorption on TM@GeSe in the end-on mode, where an oxygen atom of CO₂ attaches directly to TMs while maintaining a nearly linear shape. Cr, Cu, Pd, and Ag prefer this mode, with TM–O1 bonds ranging from 2.20 Å to 2.84 Å. The C–O1 bonds stretch slightly to 1.18 Å ~ 1.19 Å, while C–O2 bond lengths remain almost the same. As illustrated in Figure 2(b) for Cr@GeSe, charge transfer primarily happens between the C and O1 atoms, not from TM to O1, denoting local activation of the CO₂ molecule.

Strong CO₂ chemisorption occurs on TM@GeSe (where TM = Ni, Ru, Rh, and Ir) in the side-on1 mode, where only the carbon atom binds directly to the TMs. This results in two equal C–O bond lengths between 1.20 Å and 1.22 Å, and $\angle\text{O–C–O}$ bond angles between 149.23° and 157.39°. For TM like Ti, V, Mn, Fe, Co, Nb, Mo, Ta, W, Re, and Os, CO₂ adsorption happens in the side-on2 mode. Both the carbon and oxygen atoms of CO₂ bind simultaneously to TMs, causing bond angles between 128.20° and 147.46°, longer C–O1 bonds (above 1.26 Å), and slightly longer C–O2

bonds (about 1.21 Å). Charge density difference plots of Ni and Mo@GeSe show more electron transfer, indicating CO₂ molecules are effectively activated in both side-on modes. So, except for Pt, Au@GeSe (physisorption) and Cr, Cu, Pd, Ag@GeSe (local activation), the mechanism of the remaining 15 SACs was investigated further.

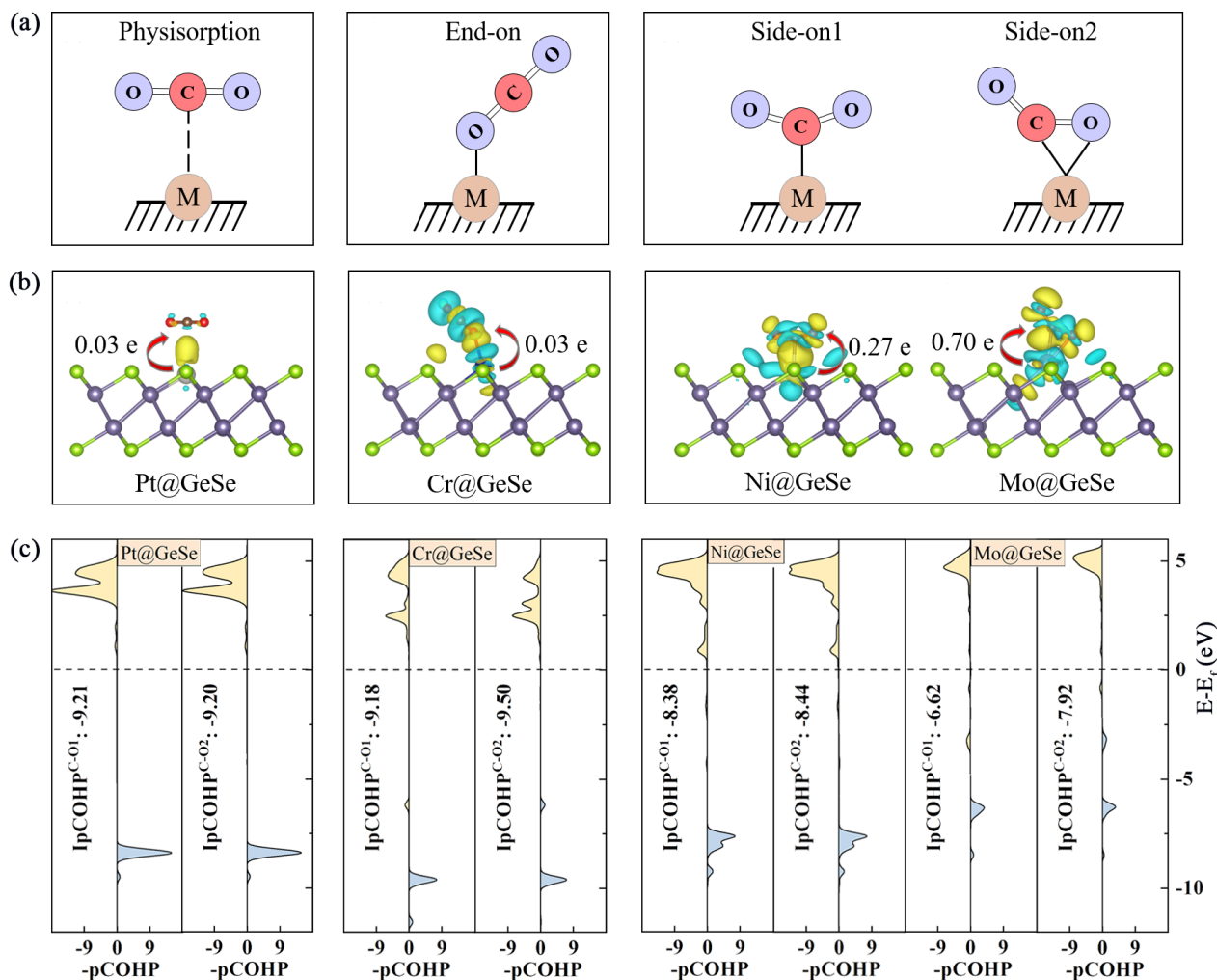


Figure 2. (a) Four adsorption configurations for CO₂ on a catalyst surface. (b) Charge density difference diagrams for CO₂ adsorption on Pt@GeSe, Cr@GeSe, Ni@GeSe, and Mo@GeSe. Yellow and cyan show charge accumulation and depletion, respectively (isosurface value: 0.005 e Å⁻³). (c) Projected crystal orbital Hamilton population (pCOHP) analysis of C–O bonds after CO₂ adsorption.

3.3 Electronic Structure of CO₂ Activation

We delved into the electronic-level mechanism of CO₂ adsorption and activation by analyzing the projected density of states (PDOS) and projected crystal orbital Hamilton population (pCOHP) of the adsorbed systems. The PDOS of examples like Pt, Cr, Ni, Mo, Ru, and Rh@GeSe, are presented in Figure S7. The hybridization between the TM-*d* and CO₂-2*p* orbitals is prominent for Ni, Mo, Ru, and Rh@GeSe, indicating a strong interaction between these SACs and CO₂ in side-

on modes. Notably, in these four systems, the antibonding states of the C–O bonds are near or below the Fermi energy level, meaning the C–O bonds are less stable and the CO₂ molecule is effectively activated, as shown in Ni, Mo@GeSe in Figure 2(c) and Ru, Rh@GeSe in Figure S7.

The integral pCOHP (IpCOHP) values for interactions between the TM and its coordinated carbon atoms (denoted as IP^{TM-C}) and oxygen atoms (IP^{TM-O1}) were calculated. As shown in Table S3, the IP^{TM-C} and IP^{TM-O1} values for both side-on modes are more negative than those for end-on and physisorption modes, indicating the interactions are stronger. Also, the IpCOHP values between carbon and both O1 (IP^{C-O1}) and O2 (IP^{C-O2}) were computed to assess the degree of activation. In the end-on and physisorption modes, IP^{C-O1} and IP^{C-O2} values are close to -9.21 eV, which is the value for free CO₂ molecules. But for both side-on modes, these values are much higher, signifying effective CO₂ activation.

3.4 Screening of Promising Catalysts

During CO₂RR, HER is a major competing side reaction. In SACs, hydrogen atoms on the metal center can poison the active site, reducing the CO₂RR efficiency. The first step in CO₂ hydrogenation forms either *OCHO or *OCOH species. Usually, a lower ΔG value means better stability and selectivity.⁶³⁻⁶⁴ To screen catalysts with high selectivity, we initially compared the ΔG values of *OCOH, *OCHO, and *H species. As depicted in Figure 3(a), among 15 screened SACs, the first protonation step favors forming *OCHO intermediates because of their lower ΔG . So, only *OCHO intermediate was considered in subsequent steps. Furthermore, except for Ir@GeSe, the other 14 TM@GeSe catalysts exhibited superior selectivity for CO₂RR over HER. This highlights the potential of using TM@GeSe as cathodes for high-efficiency CO₂RR.

We then calculated the ΔG of all intermediates for 14 SACs and summarized the most favorable reaction pathway, the potential determining step (PDS), U_{LS} , and final products in Figure 3(b). The free energy diagrams are displayed in Figure 3, S8, and S9. Notably, Ni, Ru, and Rh@GeSe stood out as excellent catalysts with low U_{LS} , similar to previously reported values.^{23-24, 65-66} Specifically, Ni and Rh@GeSe catalyze CO₂ reduction to HCOOH with U_{LS} of -0.37 V and -0.41 V, respectively, while Ru@GeSe favors CH₄ production with a U_L of -0.39 V. For more details on the hydrogenation process, see the Supporting Information.

Since CO₂RR happens in water, we studied the effect of solvent on TM@GeSe catalyst using implicit solvation models in VASPsol, with a dielectric constant of 80 for water. The results for Ni, Rh, and Ru@GeSe are presented in Fig. S11. The solvation had little impact on the free energy of most intermediates, except for *OCHOH. But the U_L decreased when considering the solvation effect. Still, this did not change the overall catalytic performance of CO₂RR on TM@GeSe much.

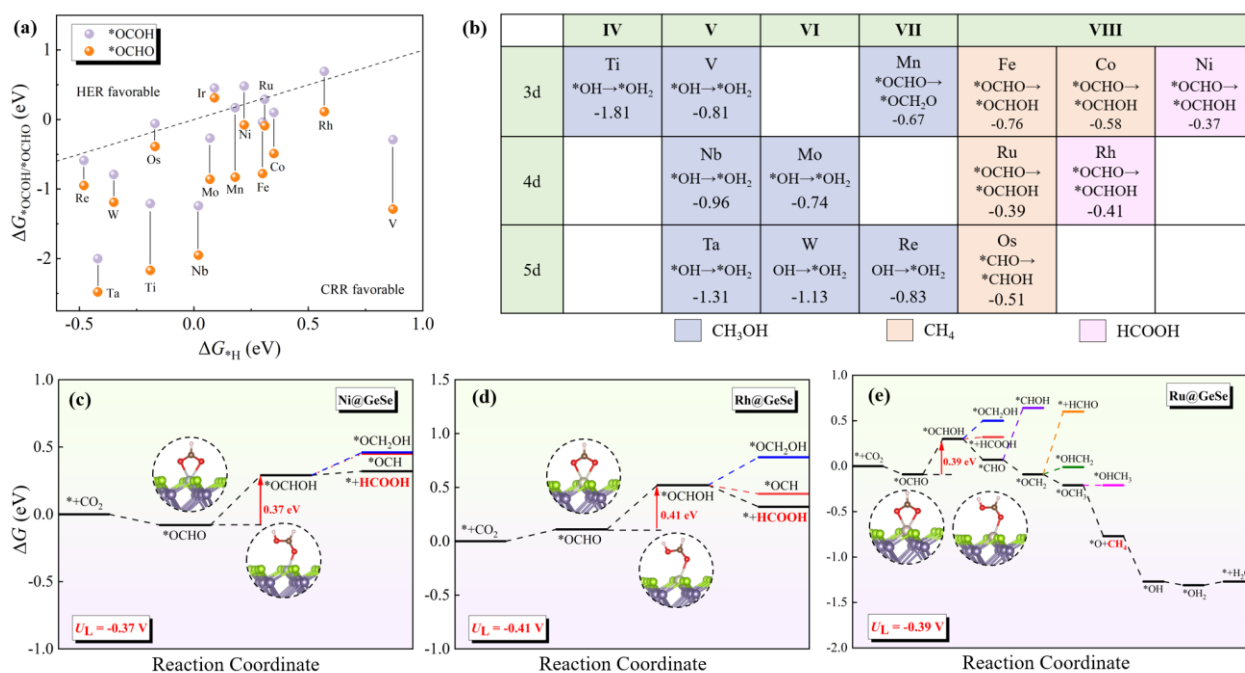


Figure 3. (a) Selectivity analysis for CO₂RR depicted as the ΔG_{*OCOHO} or ΔG_{*OCHO} compared to the ΔG_{*H} of HER. (b) Summary of the PDS, U_L s, and final products for 14 SACs. Free energy diagrams for CO₂RR on (c) Ni@GeSe, (d) Rh@GeSe, and (e) Ru@GeSe, showing intermediate structures at the initial and final states of PDS.

3.5 Descriptors Analysis in CO₂RR Process

Because the CO₂RR pathway is complex, calculating all possible reaction intermediates requires massive computational resources, especially for high-throughput screening of potential candidates. Prior studies have highlighted the importance of understanding the intrinsic activity of SACs by using the right descriptors.⁶⁷ To elucidate the structure-activity relationships, we employed specific descriptors and ML models to simplify the mechanism and facilitate the rational design of CO₂RR electrocatalysts, as shown in Figure 1(c) and 1(d).

$*OCHO$ and $*OH$ intermediates are crucial in CO₂RR, as evidenced by their strong linear correlation with other intermediates' ΔG values (Figure S12). The efficiency of product desorption depends on the adsorption strength of these intermediates. If the adsorption is too strong, it can block later reactions, increasing U_L . There is a positive correlation between each intermediate's ΔG and the U_L . For example, Ni, Ru, and Rh@GeSe catalysts, denoted by blue spheres, have U_L below -0.5 V, suggesting weaker adsorption of intermediates lead to better catalytic performance.

The 2D volcano plots in Figure 4(a-f) illustrate U_L for HCOOH, CH₄, and CH₃OH from CO₂RR as a function of $\Delta G_{*OCHO}/\Delta G_{*OH}$. Ni, Ru, and Rh@GeSe are at the top of the volcano plots for HCOOH and CH₄, indicating weaker adsorption of $*OCHO$ and $*OH$ favors these products. The data points along with the blue solid line suggest that for most TM@GeSe, the PDS in making HCOOH and CH₄ is the step from $*OCHO$ to $*OCHOH$, while for Ti, V, and Re@GeSe, the PDS for CH₄ is the step from $*OH$ to $*OH_2$. For CH₃OH production, moderate adsorption of $*OCHO$ and $*OH$ is preferred. Specifically, the PDS for pre-TM-doped GeSe is the step from $*OH$ to $*OH_2$, while

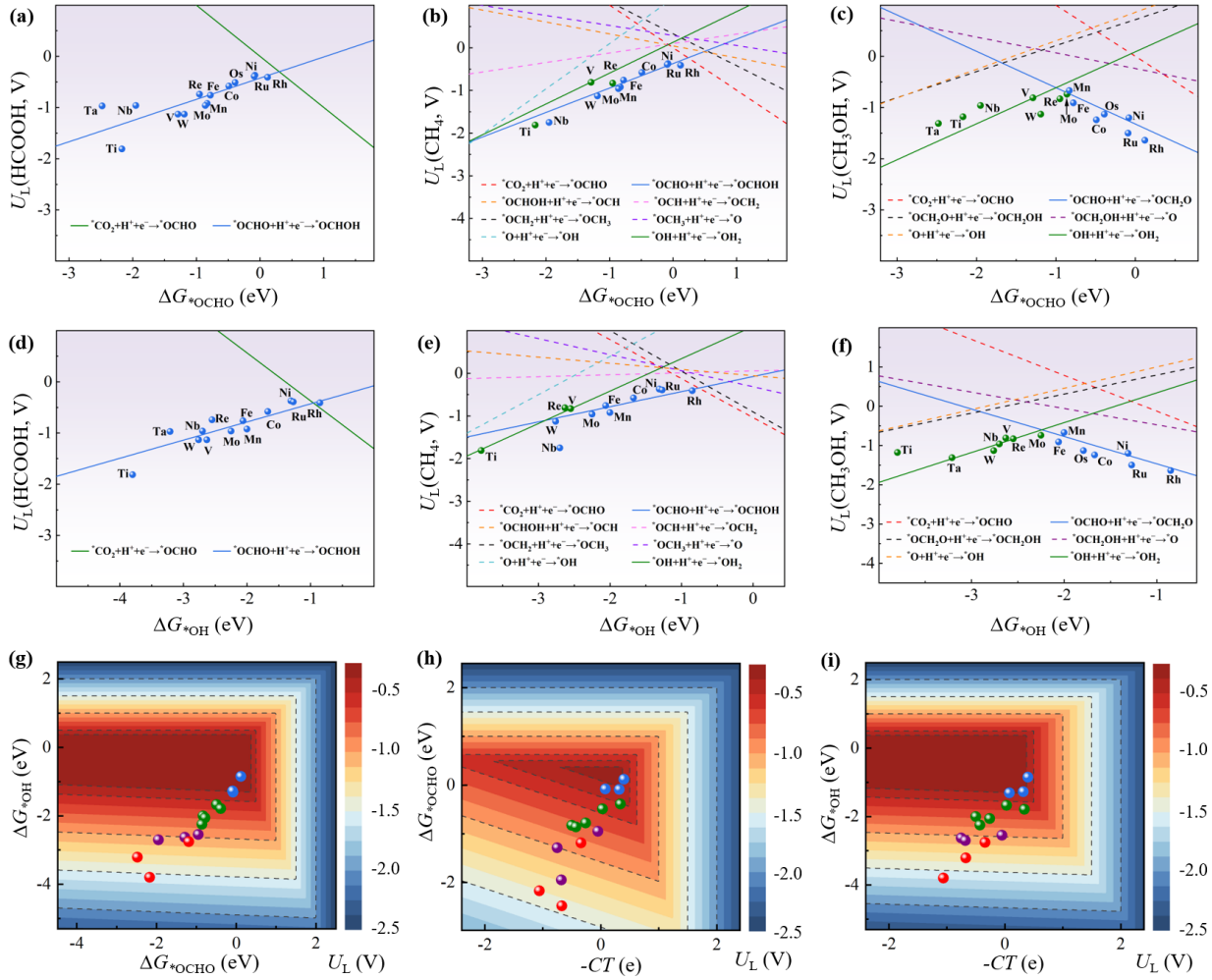


Figure 4. 2D volcano plots of U_L for CO_2RR toward (a) HCOOH , (b) CH_4 , and (c) CH_3OH as a function of ΔG^*_{OCHO} . (d-f) 2D volcano plots of U_L versus ΔG^*_{OH} . Colored lines depict key reaction steps. (g) 3D contour plots of U_L as a function of ΔG^*_{OCHO} and ΔG^*_{OH} . (h-i) U_L versus charge transfer ($-CT$), ΔG^*_{OCHO} and ΔG^*_{OH} , respectively. Colored spheres show U_L ranges.

for post-TM-doped GeSe, it is the step from $^*\text{OCHO}$ to $^*\text{OCH}_2\text{O}$. Remarkably, Mn, Mo, V, and Re@GeSe are at the volcano peak for CH_3OH production. The lowest solid lines in Figure 4(a-f) represent the basic reaction steps that limit CO_2RR activity, explaining why the second or last hydrogenation step is often the PDS in previous studies.^{11, 25} A 3D contour map in Figure 4(g) shows U_L as a function of ΔG^*_{OCHO} and ΔG^*_{OH} . The dark red triangular area in the center signifies the lowest U_L values, representing the best catalytic activity. The selected Ni, Ru, and Rh@GeSe catalysts are close to this ideal area.

The number of d electrons (N_d) in TMs is strongly related to the ΔG values of intermediates, U_L s, and products (Figure 3b and S13). Early TMs (groups IV B – VII B) with lower N_d favor CH_3OH production, while later TMs (group VIII B) with higher N_d favor CH_4 and HCOOH formation. Also, TMs with fewer N_d bind more strongly to intermediates, leading to higher U_L (Figure S13).

Steps in CO_2RR that increase entropy can be described using the number of hydrogen atoms on

carbon (H_C) and oxygen (H_O) in reaction intermediates, as well as the number of hydrogen atoms in CH_4 , CH_3OH , and H_2O species (H_S) released during the process. For example, steps like *OCH_2OH ($H_C = 2, H_O = 1, H_S = 0$) \rightarrow $^*O + CH_3OH$ ($H_C = 0, H_O = 0, H_S = 4$), *OCH_3 ($H_C = 3, H_O = 0, H_S = 2$) \rightarrow $^*O + CH_4$ ($H_C = 0, H_O = 0, H_S = 6$) show these changes.

CO_2RR is a MPET process. As illustrated in Figure S2(c), making $HCOOH$, CH_3OH , and CH_4 products requires 2, 6, and 8 proton-electron pairs, respectively. The first ($P_S = 1$), fourth ($P_S = 4$), and seventh ($P_S = 7$) steps typically have negative ΔG , meaning they are thermodynamically favorable. Especially early TMs show strong interactions between oxygen and the metal in intermediates like *OCHO , *OCH_2OH , *OCH , *OCH_3 , *O , *OH .

Charge transfer (CT) values can be used to measure the impact of MSIs on catalytic performance. As depicted in Figure 4(h-i) and S13, the ΔG of intermediates and U_L are strongly related to CT values. Early TMs, particularly Ti, V, Mn, Nb, and Ta, have CT values above 0.5, signifying they lose a lot of electrons, leading to stronger interactions with intermediates. In contrast, late TMs like Co, Ni, Ru, Rh, and Os gain electrons from the substrate, making their d -shells almost full. This means fewer empty orbitals are available for electron acceptor-donor interactions, leading to weaker adsorption of intermediates and easier product release.

To quantify the whole reaction process, we used descriptors like $IpCOHP$ values for TM-C (IP^{TM-C}), C-O1 (IP^{C-O1}), C-O2 (IP^{C-O2}), and the bond angles of O-C-O ($\angle O-C-O$). As shown in Figure S13, $\angle O-C-O$ and IP^{C-O1} values are more strongly related to the ΔG of intermediates than IP^{TM-C} and IP^{C-O2} . Along with parameters mentioned earlier, four intrinsic features of TMs (R_a , EA, IE, χ) were also used to predict free energy changes and product selectivity.

3.6 ML predictions of free energy changes and products

A total of 14 descriptors were chosen for feature engineering in ML models, as listed in Figure 5(a). Intrinsic features (IF) of TMs, including N_d , R_a , EA, IE, and χ , are listed in Table S4. Pathway-specific features (H_C , H_O , H_S , and P_S) come from the CO_2RR process. CT, IP^{C-O1} , IP^{C-O2} , IP^{TM-C} , and $\angle O-C-O$ were derived from DFT calculations. Using a dataset of 196 free energy values and 14 features (IF+DFT), we built nine common ML models: ANNs, GBR, XGBoost, LASSO, SVR, DT, ET, KNN, and RFR. R^2 , MAE, and RMSE metrics were used to evaluate the performance of models (Eqs. 1-3). A 10-fold cross-validation grid search was performed to optimize model parameters.

Among the models, XGBoost, GBR, and RFR performed the best, with high R^2 values (> 0.85) and low MAE and RMSE values (< 0.40), as shown in Figure 5 and S14. The XGBoost model was the best, with $R^2 = 0.92$, MAE = 0.24 eV, and RMSE = 0.31 eV. It also had better stability, with a higher mean cross-validation score (0.77) compared to GBR (0.74) and RFR (0.66). Features importance analysis for the XGBoost model revealed that $\angle O-C-O$, IP^{C-O1} , CT, and N_d were the

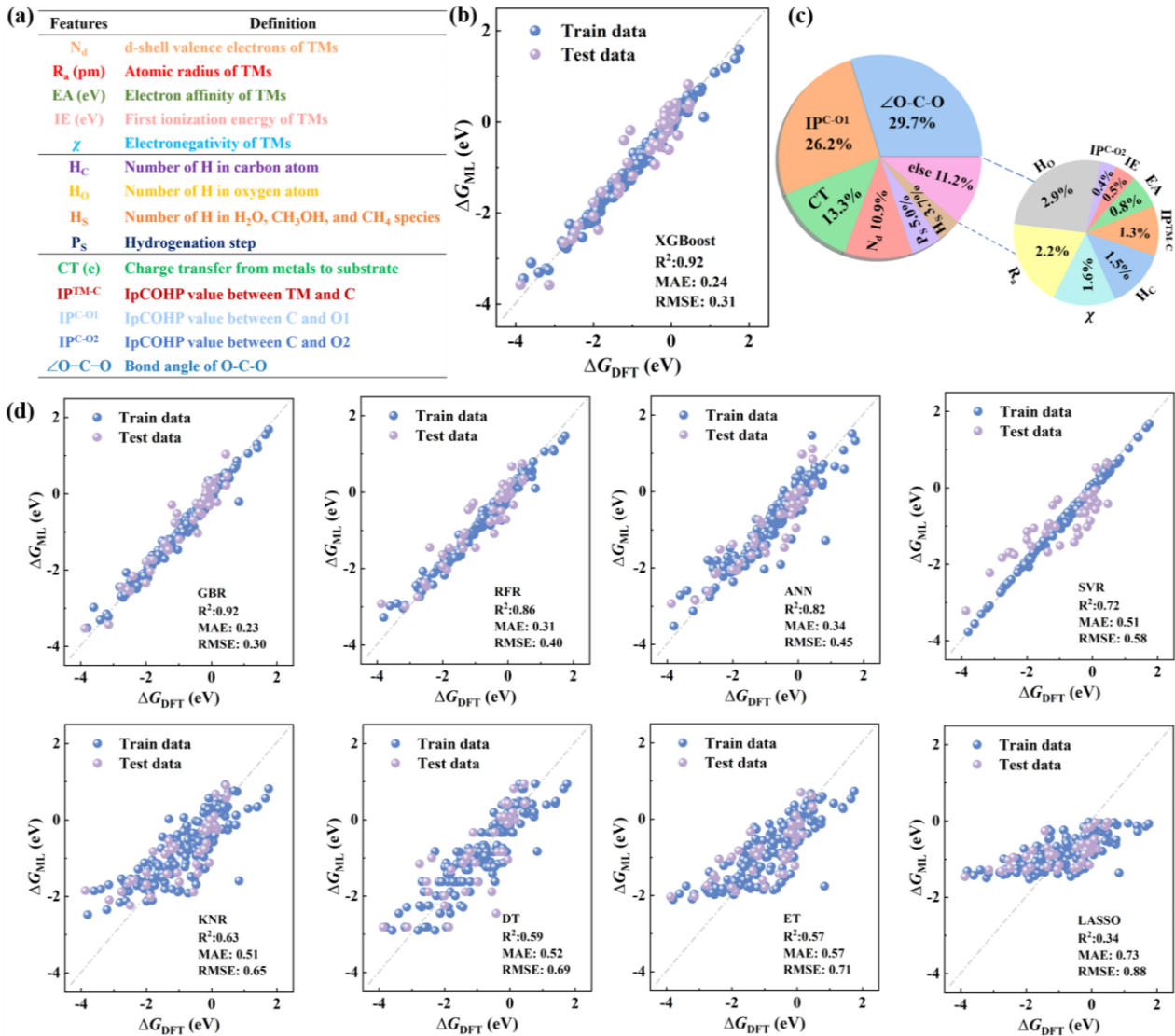


Figure 5. (a) ML model with 14 features including 9 intrinsic features and 5 DFT-based features. (b) Comparison of ΔG values between ML predictions and DFT calculations. (c) Features importance assessment for the XGBoost model. (d) Performance of the other 8 ML models in predicting ΔG .

most important features (Figure 5c and S15). Among these, the $\angle O-C-O$ and IP^{C-O1} contributed 29.7% and 26.2%, respectively, underscoring the significance of CO_2 activation in CO_2RR . This matches the descriptor analysis.

The free energy diagrams in Figure S16 compare the XGBoost model predictions using IF+DFT features with DFT results, demonstrating good agreement for each ΔG . The PDS remained the same, and the U_L showed a small error of about 0.15 eV. Also, the ML predictions identified Ni, Ru, and Rh@GeSe as promising catalysts.

To make faster predictions, we employed features that don't need DFT computations. As illustrated in Figure 6(a), DFT-based descriptors were replaced with non-DFT parameters. Specifically, the electronegativity (χ_{MC}) and valance electrons (VE_{MC}) of the metal and its first

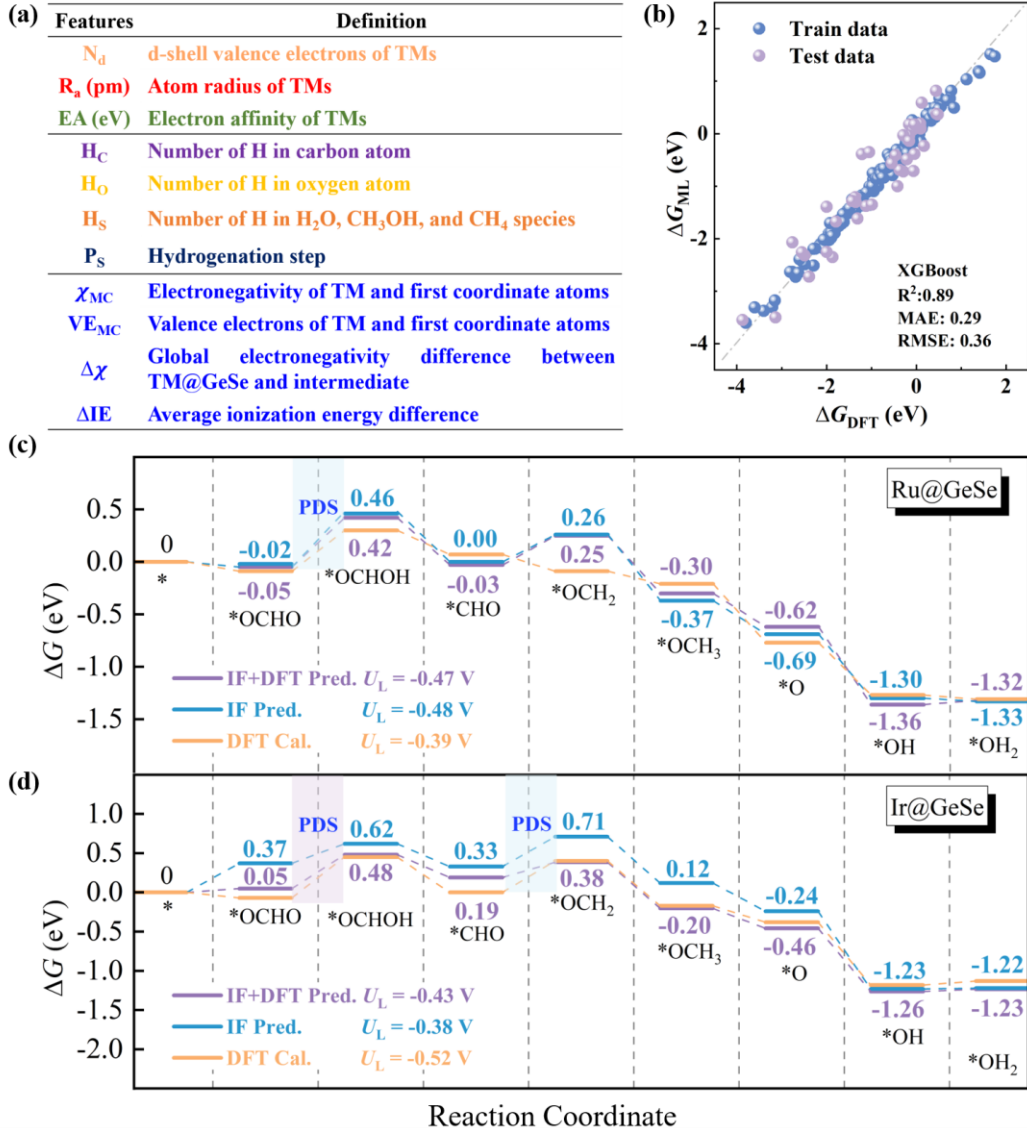


Figure 6. (a) ML model with only 11 intrinsic features. (b) Comparison of ΔG values from ML predictions using the XGBoost model with DFT calculations. Free energy diagrams for (c) Ru@GeSe and (d) Ir@GeSe. Yellow, purple, and blue lines represent DFT calculations, ML predictions with IF+DFT features, and ML predictions with IF features, respectively.

coordinated atoms were incorporated to replace the CT descriptor, which describes MSIs based on equations 4-5.⁶⁸ Furthermore, the global electronegativity difference ($\Delta\chi$) between catalysts and intermediates, and the average ionization energy difference (ΔIE) between metals and intermediates, were introduced to show the interaction strength of intermediates. In the end, 11 intrinsic features were chosen for the ML models.

$$\chi_{MC} = \chi_M + 3\chi_{Coor} \quad (4)$$

$$VE_{MC} = VE_M + 3VE_{Coor} \quad (5)$$

where χ_M and VE_M represent the electronegativity and the number of valence electrons of the metal

atom, respectively. χ_{Coor} and VE_{Coor} denote the electronegativity and the number of valence electrons of the first coordinated atoms, respectively.

$$\Delta\chi = \overline{\chi_{\text{cat}}} - \overline{\chi_{\text{Int}}} = \frac{\chi_{\text{M}} + \frac{\sum_{i=1}^{N_{\text{atom}}} N_i \chi_i}{N_i}}{2} - \frac{\sum_{j=1}^{N_{\text{atom}}} N_j \chi_j}{N_j} \quad (6)$$

where $\overline{\chi_{\text{cat}}}$ and $\overline{\chi_{\text{Int}}}$ are the average electronegativity of the catalyst and the intermediate, respectively. χ_i implies the electronegativity of each atom in catalyst except the metal atom, and χ_j refers to the electronegativity of each atom in the intermediate.

$$\Delta\text{IE} = \frac{1}{C} \sum_{i=1}^C \text{IE}_{\text{M}} - \text{IE}_i \quad (7)$$

where IE_{M} and IE_i represent the ionization energy of the metal atom and its coordination atoms (C or O) in the intermediate, respectively.

The XGBoost model utilizing only intrinsic features also performed well ($R^2=0.89$, $\text{MAE} = 0.29$ eV, and $\text{RMSE} = 0.36$ eV), as shown in Figure 6(b). The ML predictions matched well with DFT calculations (Figure S17). Features importance analysis highlighted N_{d} as the most significant descriptor (Figure S18). To exemplify the agreement between predicted and DFT-calculated ΔG values, we used Ru@GeSe as an example. In the CO_2RR process, the step from $^*\text{OCHO}$ to $^*\text{OCHOH}$ was the PDS for both the XGBoost model with IF+DFT and IF features, and the DFT calculations. Specifically, the ΔG_{max} was predicted to be 0.47 eV and 0.48 eV by the XGBoost model with IF+DFT and IF features, respectively, compared to 0.39 eV from DFT calculation, indicating good agreement with the DFT results, as seen in Figure 6(c).

To validate the model's reliability, we used Ir@GeSe as a test case. As illustrated in Figure 6(d), the ML predictions using IF+DFT features matched the DFT results better than those only IF features. Specifically, the step from $^*\text{OCHO}$ to $^*\text{OCHOH}$ was the PDS for ML predictions using IF+DFT features and DFT calculations, with ΔG_{max} values of 0.43 eV and 0.52 eV, respectively. But the PDS for ML predictions using IF features was the step from $^*\text{CHO}$ to $^*\text{OCH}_2$, with a ΔG_{max} of 0.38 eV.

To quickly predict the final product, we introduced producing probability (P_n) to differentiate HCOOH, CH_4 , and CH_3OH . As depicted in Figure 7(a), P_1 and P_2 were defined as selectivity descriptors to differentiate HCOOH from $\text{CH}_3\text{OH}/\text{CH}_4$, and CH_3OH from CH_4 . For instance, when $\Delta\Delta G_1 > 0.2$ eV, P_1 is between 0 and 0.45, favoring HCOOH. When P_1 lies between 0.55 and 1.0, $\text{CH}_4/\text{CH}_3\text{OH}$ is more likely. Similarly, when $\Delta\Delta G_2 > 0.2$ eV, P_2 falls within the range of 0 to 0.45,

favoring CH₃OH. When $\Delta\Delta G_2 < -0.2$ eV, P_2 is in the range of 0.55~1.00, favoring CH₄. Otherwise, both CH₄ and CH₃OH are possible.

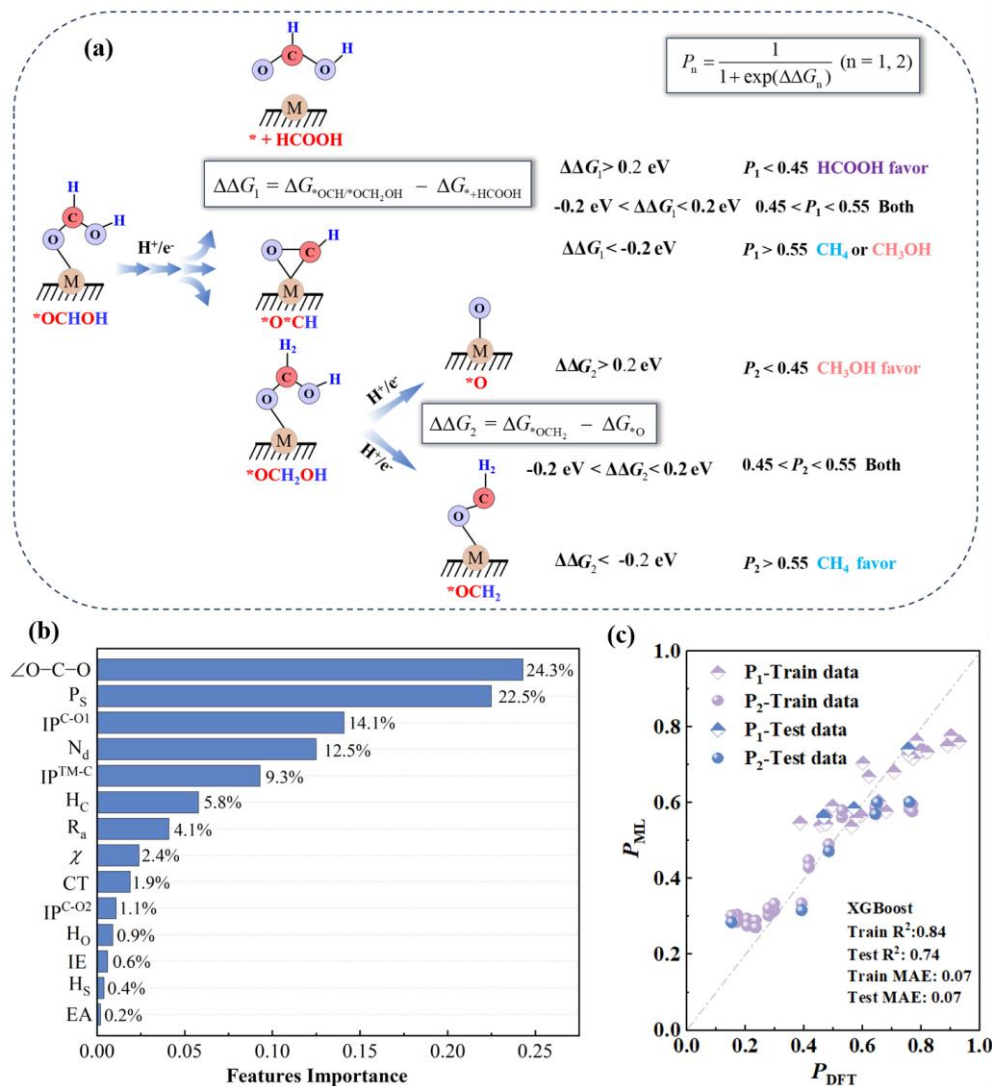


Figure 7. (a) Definition of product probability (P_n) to differentiate HCOOH, CH₃OH, and CH₄ products. (b) Features importance assessment in XGBoost model with IF+DFT features in product predictions. (c) Comparison of P values from ML predictions using the XGBR model with DFT calculations.

Next, ML models were constructed to predict the formation of products using two schemes: 14-features (IF+DFT) and 11-features (IF). The XGBoost model using 14-features made good predictions for product probabilities, with $R^2 = 0.84$ and MAE = 0.07 eV for training data, and $R^2 = 0.74$ and MAE = 0.07 eV for test data (Figure 7c). Due to the complexity of CO₂RR, the ML models still face challenges in predicting product formation. Features importance analysis revealed that $\angle\text{O}-\text{C}-\text{O}$, P_s , and $\text{IP}^{\text{C-O1}}$ were the most important, contributing 24.3%, 22.5%, and 14.1%, respectively, underscoring the importance of CO₂ activation in predicting products.

4. Conclusion

Using DFT calculations, we systematically investigated the stability, CO₂ activation, selectivity, and activity of TM@GeSe catalysts, identifying Ni, Ru, and Rh@GeSe as highly promising candidates for CO₂RR. By utilizing descriptor analysis with 14 features, the XGBoost model achieved accurate predictions of ΔG values ($R^2 = 0.92$, MAE = 0.24 eV) and product selectivity ($R^2 = 0.74$, MAE = 0.07 eV). The $\angle O-C-O$ and IP^{C-O1} features emerged as crucial for both predictions, highlighting the importance of CO₂ activation. By adopting non-DFT-based features, the XGBoost model maintained strong predictive accuracy ($R^2 = 0.89$, MAE = 0.29 eV) for rapid screening. These results not only highlight exceptional SACs for CO₂RR but also provide a scalable and efficient strategy for catalyst design.

Declaration of Competing Interest

The authors declare that they have no known competing financial interests or personal relationships that could have appeared to influence the work reported in this paper.

Data availability

The authors declare that the data will be made available on request.

Acknowledgements

This work is supported by the Natural Science Foundation of China (Grants No. 12374061) and the KC Wong Magna Foundation at Ningbo University. The computations are supported by the High-Performance Computing Center of Ningbo University.

Appendix A. Supplementary material

Supplementary data associated with this article can be found in the online version at doi:

References

1. W. H. Wang, Y. Himeda, J. T. Muckerman, G. F. Manbeck and E. Fujita, *Chem. Rev.*, 2015, **115**, 12936-12973.
2. W. Gao, S. Liang, R. Wang, Q. Jiang, Y. Zhang, Q. Zheng, B. Xie, C. Y. Toe, X. Zhu and J. Wang, *Chem. Soc. Rev.*, 2020, **49**, 8584-8686.
3. C. Zhao, L. Wang, L. Huang, N. M. Musyoka, T. Xue, J. Rabeah and Q. Wang, *J. Energy Chem.*, 2024,

- 90, 435-452.
4. Y. Guo, X. Kang, S. Gao and X. Duan, *Phys. Chem. Chem. Phys.*, 2023, **25**, 12420-12425.
 5. Z. K. Xin, M. Y. Huang, Y. Wang, Y. J. Gao, Q. Guo, X. B. Li, C. H. Tung and L. Z. Wu, *Angew. Chem. Int. Ed.*, 2022, **61**, e202207222.
 6. Z. K. Xin, Y. J. Gao, Y. Gao, H. W. Song, J. Zhao, F. Fan, A. D. Xia, X. B. Li, C. H. Tung and L. Z. Wu, *Adv. Mater.*, 2022, **34**, 2106662.
 7. X. Du, P. Zhang, G. Zhang, H. Gao, L. Zhang, M. Zhang, T. Wang and J. Gong, *Natl. Sci. Rev.*, 2024, **11**, nwad149.
 8. Y. Y. Birdja, E. Pérez-Gallent, M. C. Figueiredo, A. J. Göttle, F. Calle-Vallejo and M. T. Koper, *Nat. Energy*, 2019, **4**, 732-745.
 9. S. Nitopi, E. Bertheussen, S. B. Scott, X. Liu, A. K. Engstfeld, S. Horch, B. Seger, I. E. Stephens, K. Chan and C. Hahn, *Chem. Rev.*, 2019, **119**, 7610-7672.
 10. Y. Zang, P. Wei, H. Li, D. Gao and G. Wang, *Electrochem. Energy Rev.*, 2022, **5**, 29.
 11. L. Yu, F. Li, J. Huang, B. G. Sumpter, W. E. Mustain and Z. Chen, *ACS Catal.*, 2023, **13**, 9616-9628.
 12. L. Li, X. Li, Y. Sun and Y. Xie, *Chem. Soc. Rev.*, 2022, **51**, 1234-1252.
 13. Y. Guo, S. Yao, Y. Xue, X. Hu, H. Cui and Z. Zhou, *Appl. Catal. B-Environ.*, 2022, **304**, 120997.
 14. Y. Xue, Y. Guo, H. Cui and Z. Zhou, *Small Methods*, 2021, **5**, 2100736.
 15. X. Chen, J.-Y. Song, J. Zheng, Y.-M. Wang, J. Luo, P. Weng, B.-C. Cai, X.-C. Lin, G.-H. Ning and D. Li, *J. Am. Chem. Soc.*, 2024, **146**, 19271-19278.
 16. S. Tauster, S. Fung and R. L. Garten, *J. Am. Chem. Soc.*, 1978, **100**, 170-175.
 17. L. Wang, D. Wang and Y. Li, *Carbon Energy*, 2022, **4**, 1021-1079.
 18. S. Wang, L. Wang, D. Wang and Y. Li, *Energy Environ. Sci.*, 2023, **16**, 2759-2803.
 19. Q. Sun, C. Jia, Y. Zhao and C. Zhao, *Chin. J. Catal.*, 2022, **43**, 1547-1597.
 20. X. Kang, J. Huang and X. Duan, *Phys. Chem. Chem. Phys.*, 2022, **24**, 17155-17162.
 21. Z. Wu, X. Kang, S. Wang, Y. Song, F. Xie, X. Duan and J. Yang, *Adv. Funct. Mater.*, 2024, 2406917.
 22. W. Xun, X. Yang, Q. S. Jiang, M. J. Wang, Y. Z. Wu and P. Li, *ACS Appl. Energy Mater.*, 2023, **6**, 3236-3243.
 23. L. Ju, X. Tan, X. Mao, Y. Gu, S. Smith, A. Du, Z. Chen, C. Chen and L. Kou, *Nat. Commun.*, 2021, **12**, 5128.
 24. M. Wang, H. Shi, M. Tian, R. Chen, J. Shu, Q. Zhang, Y. Wang, C. Li, N. Wan and S. Lei, *ACS Appl. Nano Mater.*, 2021, **4**, 11017-11030.
 25. S. Zheng, C. Zuo, X. Liang, S. Li and F. Pan, *J. Energy Chem.*, 2021, **56**, 444-448.
 26. N. Luo, W. Duan, B. I. Yakobson and X. Zou, *Adv. Funct. Mater.*, 2020, **30**, 2000533.
 27. S. Lee, J. E. Jung, H. g. Kim, Y. Lee, J. M. Park, J. Jang, S. Yoon, A. Ghosh, M. Kim and J. Kim, *Nano Lett.*, 2021, **21**, 4305-4313.
 28. J. Jang, J. Kim, D. Sung, J. H. Kim, J. E. Jung, S. Lee, J. Park, C. Lee, H. Bae and S. Im, *Nano Lett.*, 2023, **23**, 3144-3151.
 29. H. G. Min, C. Lyi and Y. Kim, *Phys. Rev. B*, 2022, **106**, 205153.
 30. Z. Shu, B. Wang, X. Cui, X. Yan, H. Yan, H. Jia and Y. Cai, *Chem. Eng. J.*, 2023, **454**, 140242.
 31. C. Huan, Y. Cai, D. R. Kripalani, K. Zhou and Q. Ke, *Nanoscale Horiz.*, 2023, **8**, 404-411.
 32. V. Van Thanh, N. D. Van and N. T. Hung, *Appl. Surf. Sci.*, 2022, **582**, 152321.
 33. Z. Shu, X. Cui, B. Wang, H. Yan and Y. Cai, *ChemSusChem*, 2022, **15**, e202200564.
 34. G. Kresse and J. Furthmüller, *Phys. Rev. B*, 1996, **54**, 11169.
 35. G. Kresse and D. Joubert, *Phys. Rev. B*, 1999, **59**, 1758.

36. J. P. Perdew, K. Burke and M. Ernzerhof, *Phys. Rev. Lett.*, 1996, **77**, 3865.
37. S. Grimme, J. Antony, S. Ehrlich and H. Krieg, *J. Chem. Phys.*, 2010, **132**.
38. S. Maintz, V. L. Deringer, A. L. Tchougréeff and R. Dronskowski, *J. Comput. Chem.*, 2016, **37**, 1030-1035.
39. G. Henkelman, B. P. Uberuaga and H. Jónsson, *J. Chem. Phys.*, 2000, **113**, 9901-9904.
40. J. K. Nørskov, J. Rossmeisl, A. Logadottir, L. Lindqvist, J. R. Kitchin, T. Bligaard and H. Jónsson, *J. Phys. Chem. B*, 2004, **108**, 17886-17892.
41. K. Mathew, R. Sundararaman, K. Letchworth-Weaver, T. Arias and R. G. Hennig, *J. Chem. Phys.*, 2014, **140**, 084106.
42. B. Yegnanarayana, *Artificial Neural Networks*; PHI Learning Pvt. Ltd., 2009.
43. J. H. Friedman, *Comput. Stat. Data An.*, 2002, **38**, 367-378.
44. T. G. Dietterich, *Neural Comput.*, 1998, **10**, 1895-1923.
45. G. M. D'Angelo, D. C. Rao and C. C. Gu In *Combining Least Absolute Shrinkage and Selection Operator (Lasso) and Principal-Components Analysis for Detection of Gene-Gene Interactions in Genome-Wide Association Studies*, BMC proceedings, BioMed Central: 2009; pp 1-5.
46. D. Basak, S. Pal and D. C. Patranabis, *Neural Inf. Process.*, 2007, **11**, 203-224.
47. J. F. Magee, *Decision Trees for Decision Making*; Harvard Business Review: Brighton, MA, USA, 1964.
48. J. Pisane, R. Marée, L. Wehenkel and J. Verly In *Robust Automatic Target Recognition Using Extra-Trees*, 2010 IEEE Radar Conference, IEEE: 2010; pp 1454-1458.
49. E. A. Patrick and F. P. Fischer III, *Inf. Technol. Control.*, 1970, **16**, 128-152.
50. M. R. Segal, *Biostatistics*, 2004, 1-14.
51. F. Pedregosa, G. Varoquaux, A. Gramfort, V. Michel, B. Thirion, O. Grisel, M. Blondel, P. Prettenhofer, R. Weiss and V. Dubourg, *J. Mach. Learn. Res.*, 2011, **12**, 2825-2830.
52. H. Shu, D. Zhou, F. Li, D. Cao and X. Chen, *ACS Appl. Mater. Inter.*, 2017, **9**, 42688-42698.
53. M. Pizzochero and O. V. Yazyev, *Phys. Rev. B*, 2017, **96**, 245402.
54. X. Kang, Q. Fang, H. Yin, A. Du and X. Duan, *Mol. Catal.*, 2024, **568**, 114477.
55. E. Olsson, G. Chai, M. Dove and Q. Cai, *Nanoscale*, 2019, **11**, 5274-5284.
56. J. Ou, X. Kang and X. Duan, *Nanoscale*, 2022, **14**, 12823-12829.
57. G. Gao, Y. Jiao, E. R. Waclawik and A. Du, *J. Am. Chem. Soc.*, 2016, **138**, 6292-6297.
58. X. Cui, W. An, X. Liu, H. Wang, Y. Men and J. Wang, *Nanoscale*, 2018, **10**, 15262-15272.
59. X. Kang, Z. Chu and X. Duan, *Appl. Surf. Sci.*, 2021, **560**, 149667.
60. X. Wang, Q. Zhang, W. Hao, C. Fang, J. Zhou and J. Xu, *J. Mater. Chem. A*, 2022, **10**, 15036-15050.
61. S. Cao, H. Chen, Y. Hu, J. Li, C. Yang, Z. Chen, S. Wei, S. Liu, Z. Wang, D. Sun and X. Lu, *Chem. Eng. J.*, 2023, **461**, 141936.
62. X. Guo, J. Gu, S. Lin, S. Zhang, Z. Chen and S. Huang, *J. Am. Chem. Soc.*, 2020, **142**, 5709-5721.
63. A. Michaelides, Z. Liu, C. Zhang, A. Alavi, D. A. King and P. Hu, *J. Am. Chem. Soc.*, 2003, **125**, 3704-3705.
64. J. Cheng, P. Hu, P. Ellis, S. French, G. Kelly and C. M. Lok, *J. Phys. Chem. C*, 2008, **112**, 1308-1311.
65. M. Umer, S. Umer, R. Anand, J. Mun, M. Zafari, G. Lee and K. S. Kim, *J. Mater. Chem. A*, 2022, **10**, 24280-24289.
66. W. Zhou, X. Kang, S. Gao and X. Duan, *Appl. Surf. Sci.*, 2024, **665**, 160299.
67. J. Zhao, P. Zhang, T. Yuan, D. Cheng, S. Zhen, H. Gao, T. Wang, Z. Zhao and J. Gong, *J. Am. Chem. Soc.*, 2023, **145**, 6622-6627.
68. Q. Zhu, Y. Gu, X. Liang, X. Wang and J. Ma, *ACS Catal.*, 2022, **12**, 12336-12348.